3-4 (2022) 100013

Contents lists available at ScienceDirect

IPEM-Translation

journal homepage: www.elsevier.com/locate/ipemt

Full Length Article

# Detection accuracy of I-125 seeds and needle tips, in MRI prostate tissue mimicking material: Phantom design, fabrication, and testing

Sarah Wilby [a,b,*], Antonio De Stefano [a], Antony L. Palmer [a,b], Wojciech Polak [a,b], Petko Petkov [b], Andrea Bucchi [b]

[a] Medical Physics Department, Portsmouth Hospitals University NHS Trust, Portsmouth PO6 3LY, United Kingdom
[b] School of Mechanical and Design Engineering, Faculty of Technology, University of Portsmouth, Anglesea Building, Anglesea Rd, Portsmouth, PO1 3DJ, United Kingdom

ARTICLE INFO

*Keywords:*
Brachytherapy
MRI
I-125
Phantom
Prostate

ABSTRACT

Accurately identifying needle tip and seed positions for low dose rate prostate brachytherapy on MRI images is challenging. Uncertainties in locating needle tip positions can lead to misplacement of seeds compared to planned coordinates. Furthermore uncertainty in establishing true seed positions on the images, leads to uncertainty in the dose distributions.

In this study, a novel phantom has been designed for the analysis of I-125 seed and needle tip detection and tip image distortion. The phantom utilises a gel that mimics prostate tissue in MRI, to evaluate the uncertainty in establishing seed and needle tip positions. Reults are reported for the IsoSeed (Bebig) source, in clinically relevant seed arrangements, and for a novel nitinol needle.

The choice of MRI sequence impacts the accuracy of detecting the needle tips and seeds. This is most prevelant when the seeds are in clusters, at the boundary of the prostate and at 90° to the long axis of the scanner. Detected needle tip position, when the MRI metal artefact correction algorithm was used, was measured consistently inferior to the actual position (mean tip at -2.3 ± 1.5 mm ($k = 2$), $p = 0.03$).

We have demonstrated the design of a phantom that can be used to quantitatively assess seed and needle tip positions simultaneously, to establish the accuracy of detection, or presence of artefacts on MRI.

## 1. Introduction

Low dose rate (LDR) permanent implant brachytherapy (BT), is a routinely used and well established treatment technique for low and intermediate risk prostate cancer [1]. It is common for the implant of I-125 seeds to be guided by live ultrasound (US) imaging. An essential part of the BT procedure, to ensure high quality dosimetry, is identifying the tip of the needle and final source positions accurately. During an LDR BT implant, the computerised planning system can be used to continually update the intended seed positions in the next needle, based on the localisation of seeds already implanted, to maintain acceptable optimised dose distributions. These implanted seed locations are established from the live imaging modality, i.e., dynamic dose calculation [2]. Any error in identifying the needle tip or the delivered seed position introduces uncertainty in the dosimetry and ultimately impacts on the quality of the treatment for the patient. Using Transrectal ultrasound (TRUS), a seed placement accuracy of 3–6 mm in-vivo is expected [3] however not all of these seeds can be identified on the live US [2], hindering the dynamic dose calculation. The superior soft tissue visualisation of prostate anatomy on MRI combined with the advantage of being able to acquire images at any angle, provides motivation to carry out these implants guided by live MRI [4]. This is an active field of research, as demonstrated in a recent review of MRI-guided robotic prostate brachytherapy [5]. The American Association of Physicists in Medicine (AAPM) specifications for image guided robotized BT detail a spatial accuracy of 1 mm (standard deviation (SD) 0.5 mm) for the placement of seeds in a phantom [3] and 0 - 2 mm in-vivo. If dynamic dose calculation is to be part of the MRI-guided robotic brachytherapy procedure, then understanding the accuracy of localising needles and seeds should be investigated for the specific MR scanner and imaging sequences being used.

In previous work, Liu et al. demonstrated a 'blooming' artefact at the tip of conventional LDR seed-loading titanium needles in MRI, and demonstrated that the size of the artefact is dependant on the imaging parameters [6]. Seed identification in MRI is also challenging since the seeds appear as 'black voids' against the dark grey appearance of prostate tissue. Nosrati et al. published on seed detection in a prostate tissue

* Corresponding author at: Medical Physics Department, Portsmouth Hospitals University NHS Trust, Portsmouth PO6 3LY, United Kingdom.
*E-mail address:* UP914718@myport.ac.uk (S. Wilby).

https://doi.org/10.1016/j.ipemt.2022.100013
Received 5 July 2022; Received in revised form 8 November 2022; Accepted 14 November 2022
Available online 15 November 2022

**Nomenclature**

| | |
|---|---|
| LDR | = Low Dose Rate |
| BT | = Brachytherapy |
| US | = Ultrasound |
| TRUS | = Transrectal Ultrasound |
| AAPM | = American Association of Physics in Medicine |
| SD | = Standard Deviation |
| PTMM | = Prostate tissue mimicking material |
| IGC | = Internal Grid Component |
| ISC | = Internal Seed Component |

mimicking phantom with similar T1 and T2 relaxation times to prostate. They used an optimised quantitative susceptibility mapping technique to demonstrate the detection of seeds in MRI. Their results showed a comparable accuracy in seed centroid detection on MRI compared to commercially available CT-based seed detection algorithm [7,8]. Wachowicz et al. characterized the susceptibility artefact around a single prostate seed in porcine gel with the aim of establishing where the seed is positioned within the image distortion patterns [9] and in a later publication considered the artefact effect when increasing the magnet strength from 1.5 T to 3.0 T [10].

Whilst there is a vast amount of scientific and clinical experience in planning LDR prostate treatments on US images, there is limited knowledge on potential pitfalls to planning on MRI. This work aims to investigate the accuracy and limitations of LDR prostate brachytherapy in MRI and differs from previous work published in a few ways: (a) a novel phantom has been designed to closely match the clinical situation: a cylindrical phantom with prostate tissue mimicking material (PTMM) with surrounding fatty tissue substitue, in combination with the MR pelvic coil for scanning; (b) complex seed distributions have been used to more accurately simulate the clinical situation; (c) a metal artefact correction algorithm was included in the analysis; and (d) novel Nitinol needles have been used as opposed to the more commonly used Titanium needles.

## 2. Materials and methods

### 2.1. Phantom design and fabrication

The phantom was designed to hold three test objects inside an external cylinder containing oil. PTMM gel was used to surround the seeds and needles. Fig. 1 shows the internal components before filling with oil. The phantom was designed to hold the PTMM within a 3D Acrylic grid for analysis of needle tip artefacts. Throughout the paper this is referred to as the IGC (internal grid component). The phantom also housed a cylindrical stack of PTMM for the analysis of seed positions, termed the internal seed component (ISC). The housing of the phantom was a transparent acrylic cylinder (200 mm diameter x 300 mm length, 5 mm wall thickness), large enough to hold the internal objects away from the edges where image artefacts may be present. A base plate printed in ABS-M30 was used to support the internal phantom components (Fig. 1). An array of regularly spaced 5 × 5 × 10 mm openings were printed into the top surface of the base plate, allowing the IGC and the ISC to be moved into different positions.

For the IGC, empty boxes (each 15 ± 0.2 $mm^3$), in a 3 × 3 × 3 arrangement, were cut from acrylic sheets. To ensure the needles could be inserted straight and in the centre of the cubes, a needle guide was printed in ABS-M30. The assembled grid with needles in place can be seen in Fig. 3. The grid was filled with the PTMM, and an acrylic stand was designed to fix the centre of the grid at the centre of the cylindrical phantom. A single cube and stand were made, termed a gridlet, with a printed guide to hold the needle at 45° in the x-y plane (see Fig. 4) with the tip at the centre of the cube.

For the ISC, a mould was cut to produce eight PTMM discs, each 60 mm diameter and 5 mm thick. Laminated paper templates were designed to embed seeds in pre-configured arrangements on the surface of five of the PTMM discs within the ISC, the remaining three discs were used without seeds. The moulds were positioned on the templates,

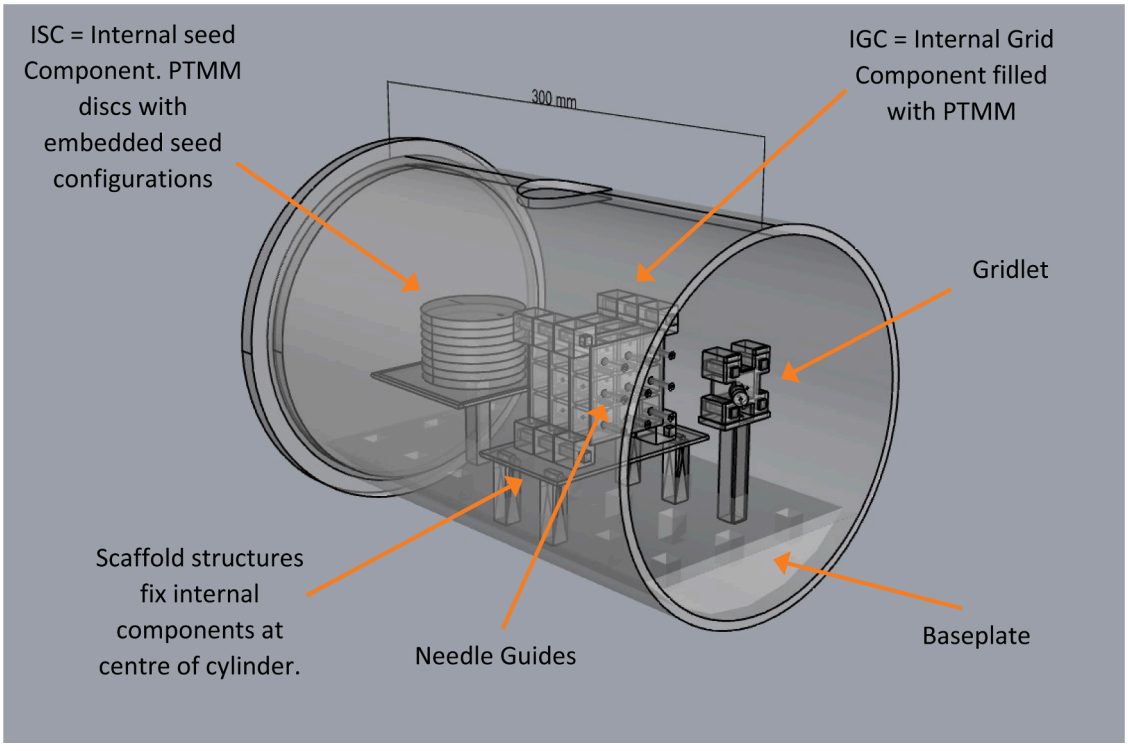


**Fig. 1.** Schematic of phantom with main parts labelled and one end of cylinder left open to visualise internal objects.

aligned with notches and the seeds were carefully placed using tweezers. The PTMM gel was slowly poured into the moulds, to minimise disruption of the seed positions. The gel was scraped along the top of the mould to ensure a flat surface and left to set before wrapping in clingfilm and storing in the fridge to avoid shrinkage. The templates were designed to test the following clinical scenarios (Fig. 5):

a. Angled seeds (regularly spaced, clustered and touching);
b. Resolving seeds laterally, with different spacing and when placed at the periphery of the prostate;
c. Well-spaced angled seeds between 0° and 90°;
d. Regularly spaced seeds in a strand;
e. Seeds touching vertically in a row and horizontally.

The discs were stacked on top of each other to form a cylinder, representing a large prostate volume (~75 cc) for LDR prostate brachytherapy. The seeds were cylindrical, non-radioactive 'dummy' seeds (IsoSeed, Bebig). A simple acrylic stand was made to hold the centre of the ISC at the centre of the external cylinder.

### 2.2. PTMM materials selection

The PTMM ingredients (Carrageenan Kappa, Agar, (www.specialingredients.co.uk), $GdCl_3$ (www.thermofischer.com) and water, 3 g, 0.8 g, 0.8 mg and 96 g per 100 g, respectively) were used. These were selected to give clinically relevant T1 relaxation times on 1.5 T MRI (T1 measured = 1400 ± 96 mS, T1 clincial ~1317 ± 85 mS for 1.5 T [11]). The T1 relaxation time was measured from the MR images based on a calibration curve established from the Eurospin calibration phantom (www.leedstestobjects.com). The formulation was based on a modification of the recipie from Stich et al. [12] and included the principle ingredients listed in a recent review paper on tissue mimicking materials [13]. T1 MR imaging alone was considered because clinically this provides a homogenous image of prostate tissue, simplifying seed detection. T2 weighted images are excellent for visualising the anatomy but were not of interest in this study because the inhomogenous appearance of the prostate on T2 images makes it less suitable for seed or needle tip detection.

### 2.3. MR image acquisition

MRI images of the assembled phantom were acquired using a Siemens Area 1.5 T scanner. The sequences used are detailed in Table 1. Series 3 (S3) is a typical sequence used for clinical diagnostic imaging of the prostate at our centre. S4 was a simple modification of this, reducing the slice thickness to see how this effected the accuracy of seed and needle tip detection. S2 included the metal artefact correction algorithm SEMAC. S1 allowed a smaller slice width using a volumetric acquisition (VIBE) and a water-fat separation (DIXON).

### 2.4. Image analysis

An in-house Matlab script was written to assist in determining the coordinates of the seeds. Some movement of seeds from their template position was anticipated during preparation of the gel discs. To account for this in the analysis, photographs of each disc were acquired, just prior to assembing the full phantom and MR imaging, using a Samsung Galaxy A71 phone camera, model SM-A715F/DS. In Matlab, the user identified the seed tips, from which the script calculated the centre of each seed relative to the local origin, and the angle of the seed relative to the Z-axis (Fig. 5). This procedure was carried out for the photographs and the MR datasets, and the difference between the two was analysed. For one gel slice in each image set, the measurements were repeated for all available seeds.

Camera distortion was analysed in Matlab using two methods, (1) photographs of graph paper and (2) aspect ratio of the gel disc photographs. Distortion was accounted for in the uncertainty budget (Section 3.5).

For the needle analysis, ImageJ was used. Images were scaled using the 'pixel per mm' values from the DICOM header files and verified using a known dimension on the Acrylic grid. Image profiles of grey value versus distance were taken in the x and z directions (Fig. 6). Measurements were taken from line profiles acquired in the left, central and right cubes of the grid. The oblique needles were positioned within a single cube with their tip at the centre. In all cases, oblique and parallel, the needle tips were fixed at the very centre of the cube and the expected (x, z) coordinate was (0,0).

### 2.5. Statistical analysis

For the statistical analysis Shapiro-Wilk tests for normality were performed on all datasets. This was followed by the non-parametric Friedman test to identify (a) any statistically significant differences between actual and measured seed / needle coordinates and angles and (b) any statistically significant differences between the results for the different MRI series. The Friedman test was chosen because it is suitable for non-normal, paired data with more than two groups. Any significant differences detected at the 95% confidence interval were compared pairwise using the post-hoc Dunn-Bonferroni method [14].

## 3. Results

### 3.1. Difference between measured seed coordinates and angles for all MRI series

The difference between the expected seed coordinate or angle versus that measured from the MRI series, is denoted by Δx, Δy, Δz and ΔØ and presented in Fig. 7.

In the x-z plane, all differences > 2.0 mm between measured and actual seed coordinates are for seeds in clusters.

Sahpiro-Wilk tests identified datasets significantly different to the normal distribution ($p < 0.05$ at the 95% confidence level). The Freidman test for non-parametric analysis did not demonstrate any significant difference in the seed coordinates or angle between any of the four MRI series tested. However, it did identify a significant difference between actual and measured seed coordinates and angle. Post-hoc analysis showed that this was significant ($p < 0.001$) for Δz, Δy and angle and insignificant for Δx ($p = 0.06$).

**Table 1**
MRI sequence parameters. (SW: Slice width mm, TR: Repetition time ms, TE: Echo time ms, #N: Number of averages, Freq: Imaging frequency Hz, ETL: Number of Echos, Dist: Gap between slices mm, Coil: Transmit coil name, PED: In-plane phase encoding direction).

| Series | Protocol Name | Scanning Sequence | SW (mm) | TR (ms) | TE (ms) | Dist. (mm) | ETL | Rows | Columns | PED |
|---|---|---|---|---|---|---|---|---|---|---|
| S1[1] | Vibe_dixon | GR | 1 | 6.78 | 2.39 | 0 | 2 | 3552 | 280 | Row |
| S2 | tse_semac | SE | 2 | 1710 | 6.6 | 2 | 9 | 320 | 320 | Row |
| S3 | tse_3mm | SE | 3 | 644 | 10 | 3 | 3 | 512 | 512 | Col |
| S4 | tse_1.2mm | SE | 1.2 | 1280 | 12 | 1.2 | 3 | 512 | 512 | Col |

[1] For all series: $\#N = 1$, Coil = Body, Freq = 63.68 Hz.

Y is perpendicular to the acquisition plane (x-z) and results show that maximum values for Δy increase with the acquisition slice width (Δy = 2.0, 2.4, 3.0, 5.0 mm; slice width = 1.0, 1.2, 2.0, 3.0 mm respecteively).

ΔØ is within +/- 10° for all MRI data series tested and max ΔØ is 29°

S2, utilising the SEMAC algorithm, has the lowest mean Δz of the four MRI series tested (see Fig. 7). In the x-z plane, the results show that the accuracy of seed detection when imaged with S2 results in a mean difference from expected position of 0.6 ± 0.25 mm (SD = 0.5 mm; range 0.0 to 2.1 mm). Removing seeds in clusters reduces the range to 0 to 1.9 mm ± 0.25 mm.

### 3.2. Seed position observations

The choice of MRI sequence affects how easy, or difficult it can be to identify a seed at the boudary of the PTMM/oil. In Fig. 8c, imges acquired with S2, the seed at the boundary is visible. In Fig. 8b, imges acquired with S4, the seed at the boundary is not visible

The photograph in Fig. 8d shows a single seed perpendicular to the Z-Y plane. In the corresponding MR image (Fig. 8e), this could be mistaken for two seeds, due to an artefact effect.

Fig. 8f (MR without metal artefact correction) and Fig. 8g (MR with metal artefact correction) show the same seed slice. However, the orientation of the top two seeds could mistakingly be identified as illustrated by the blue arrows (Fig. 8f) as opposed to their true position identified in Fig. 8g.

Fig. 9 demonstrates the difficulty of detecting seeds in clusters. In the clustered seeds, circled in Fig. 9, there are 3 and 2 seeds seen in the photographs, a and c. In the equivalent MR images, b and d, there appear to be just 2 and 1 seeds, respectively.

### 3.3. Nitinol needle tip

Table 2 gives the average needle tip position compared to expected (mm) for parallel and oblique needles relative to the x and z axis, and for each of the MRI series.

Table 2 shows that all parallel needles in S2 appeared shorter than the equivalent image in any other series. Post-hoc Dunn-Bonferroni analysis showed that this was significantly different to the expected z position with $p = 0.031$. This effect was not seen for S2 when the needle was at a 45° angle to the Z axis.

The shift in the x direction for series 1, noted in Table 2, is also significantly different from the expected result with $p < 0.001$.

No blooming at the tip of the Nitinol needles was identified for any MRI series.

No distortion of the 15 $mm^2$ grid immediately surrounding the needle tips was present, for all needle positions and all MRI series.

### 3.4. Repeatability & uncertainties

The full uncertainty budget seed localization and needle tip localization can be found in Tables 3 and 4, respectively. An explanation of each uncertainty is given below [15]:

**Table 2**
Accuracy of identifying needle tips for parallel and oblique needles.

| Series | Needle tip position vs expected mm (parallel to Z-axis) | | Needle tip position vs expected mm (oblique, 45° to Z axis) | |
|---|---|---|---|---|
| | x | z | x | z |
| **1** | −1.3 (±1.8) | −0.1 (±1.8) | −0.4 (±1.8) | 1.0 (±1.8) |
| **2** | −0.7 (±1.5) | −2.3 (±1.5) | 0.4 (±1.5) | −1.0 (±1.5) |
| **3** | −0.8 (±0.9) | 1.6 (±0.9) | −0.1 (±0.9) | −0.5 (±0.9) |
| **4** | −0.8 (±0.9) | 1.2 (±0.9) | 0.1 (±0.9) | −0.4 (±0.9) |

**Table 3**
Uncertainty budget for seed localisation, split by MRI series.

| Source of uncertainty | MRI series | Value (± mm) | Divisor | Standard uncertainty (± mm) |
|---|---|---|---|---|
| (1) u for repeated MRI/ MRI analysis | S1 | 0.03 | 1 | 0.03 |
| | S2 | 0.08 | | 0.08 |
| | S3 | 0.10 | | 0.10 |
| | S4 | 0.12 | | 0.12 |
| (2) u for repeated photo/photo analysis | N/A | 0.04 | 1 | 0.04 |
| (3) Distortion uncertainty | N/A | 0.14 | $\sqrt{3}$ | 0.08 |
| (4) Origin uncertainty | N/A | 0.11 | 1 | 0.11 |
| Expanded uncertainty ($k = 2$) | S1 | | | 0.29 |
| | S2 | | | 0.33 |
| | S3 | | | 0.35 |
| | S4 | | | 0.37 |

**Table 4**
Uncertainty budget for needle positions, split by MRI series.

| Source of uncertainty | MRI series | Value (±mm) | Divisor | Standard uncertainty (± mm) |
|---|---|---|---|---|
| (5) Resolution | S1 | 0.90 | 1 | 0.90 |
| | S2 | 0.70 | | 0.70 |
| | S3 | 0.40 | | 0.40 |
| | S4 | 0.40 | | 0.40 |
| (6) Manufacturing uncertainty | N/A | 0.20 | $\sqrt{3}$ | 0.12 |
| (7) Needle indertion depth uncertainty | N/A | 0.25 | $\sqrt{3}$ | 0.14 |
| Expanded uncertainty ($k = 2$) | S1 | | | 1.84 |
| | S2 | | | 1.45 |
| | S3 | | | 0.88 |
| | S4 | | | 0.88 |

1. Standard uncertainty (U) of repeat measurements on the same MRI slices: 17 MR slices were analyzed twice each (to give 34 samples), with the difference between all seed positions in x and z being recorded.

$$U = \sigma / \sqrt{n} \quad (1)$$

where σ is the standard deviation and n is the number of samples.

2. Standard uncertainty (U) of repeat measurements on the same photos: All seed positions on a single photo were analysed twice, with the difference between the seed positions in x and z being recorded (see Eq. (1))
3. Standard uncertainty in image distortion from photos ($U_p$): Distortion lies between 0 and 0.9%. Applied to the minimum and maximum distance of a seed from the origin (i.e., 0 and 30 mm), this equates to an uncertainty range of 0 – 0.27 mm. Assuming a rectangular distribution, half-width (*h)* equates to 0.14 mm Eq. (2).

$$U^p = h/\sqrt{3}. \quad (2)$$

4. Standard uncertainty (U) in position of origin: The origin was established twice for six different MRI slices, with the difference between coordinates in both x and z directions being recorded (see Eq. (1)).
5. Standard uncertainty (U) of repeat measurements on the same MRI slices: Measurements were repeated 12 times on each dataset (see Eq. (1)).

6. Manufacturing uncertainty ($U_m$): A manufacturing uncertainty (u) of 0.2 mm was estimated for the IGC and gridlet. Assuming a rectangular uncertainty distribution,

$$U^m = u/\sqrt{3}. \quad (3)$$

7. Needle insertion depth uncertainty (Un): An uncertainty (u) of 0.25 mm was estimated for the needle insertion depth and a rectangular uncertainty distribution (see Eq. (3)).

## 4. Discussion

Utilising MR imaging that is parallel to the longitudinal axis of the seed enables accurate detection of the seed centroid along its short axis (x). This was shown to be the case for all MRI sequences tested. Detecting the centre of the seed in the long axis (z) and the seed angle, is more challenging due to the image artefact at the tips of the seeds. Accurate detection in the y axis is directly related to the slice width and will be affected if the imaging plane is not perfectly parallel to the seeds.

It is worth noting that in the x-z plane (see Fig. 2 for the coordinate system), the accuracy of seed detection is improved with the metal artefact correction algorithm. Conversely, the results of the needle tip detection consistently show that the needle tip appears inferior of its actual position when the metal artefact correction algorithm is used. Therefore, for accurate LDR prostate brachytherapy planning it may be necessary to consider separate imaging sequences for needle insertion and seed detection.

A 'worst case scenario' can be considered whereby the seeds are deposited 2 mm in the Z direction from their intended position due to incorrect localisation of the needle tip, combined with a further 2 mm error in localising the seed centre in Z. This could lead to an error in the D90 (Dose to 90% of the prostate) estimation of between 10 – 15% and an error in the V100 (prostate volume receiving 100% of the dose) estimation of up to 5%.

In the literature it has been demonstrated that seed angle has no statistically significant difference on prostate dose metrics but can result in organ at risk differences averaging 2% [16].

Interesting observations were found in this study from looking closely at the MR images themselves rather than solely the numerical data. Firstly, there is a potential issue when using the metal artefact correction when seeds are positioned at 90° to the y-axis (i.e., parallel to the x-axis). In this situation a single seed can appear as two seeds. For a standard rigid needle, template guided implant, this is an unlikely occurrence. However, the likelihood of this event occurring when using minimal insertion points and steerable needles is much greater [19]. Secondly, when seeds are clustered, it can be difficult to resolve them as two separate seeds. Thirdly, placing seeds right on the boundary of the prostate can make seed detection very challenging. These scenarios can be considered basic rules that can be applied as objectives in any MRI guided LDR planning software.

According to the AAPM Task Group 128 [17], the error in measured axial and lateral resolution on ultrasound, should be less than 2 mm or 3 mm, respectively in a phantom containing objects that mimic seeds, which are well spaced. Our results show that this level of accuracy is achievable in MRI when seeds in clusters are removed, for all sequences except S3, which had the largest slice width, 3 mm. The smallest mean Δx and Δz for all seeds was identified with S2, which uses the metal artefact correction. However, S1, using a volumetric acquisition with 1 mm slice width and water-fat separation, gave the smallest range in Δx and Δz, within 2 mm for all seeds including those in clusters.

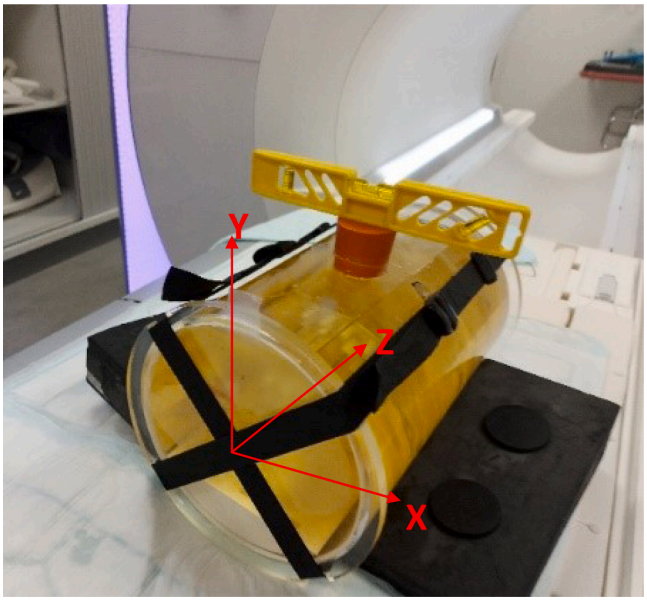


**Fig. 2.** Photo of filled and sealed phantom on MR scanner.

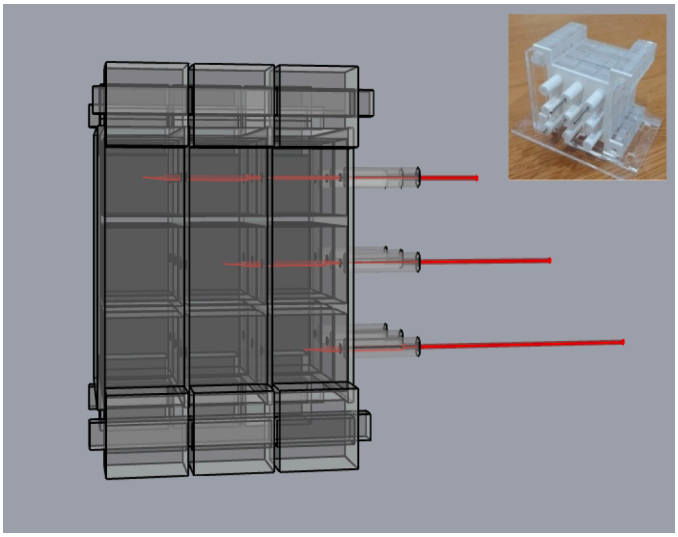

**Fig. 3.** Needles fixed at center of cubes, which are filled with PTMM (needles in red for clearer visualisation only).

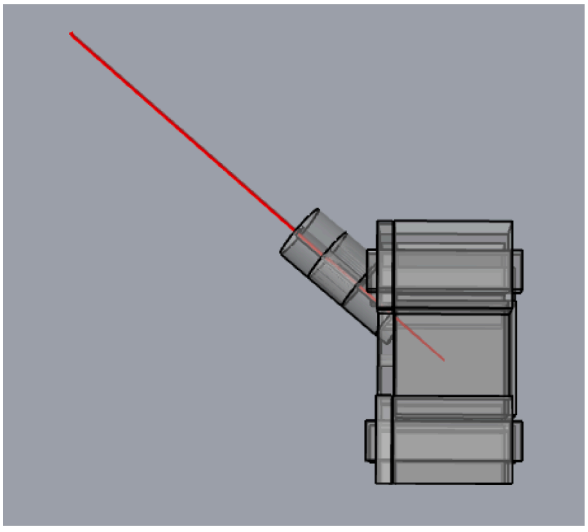

**Fig. 4.** Birds-eye view of gridlet with angled needle fixed at center of PTMM filled cube.

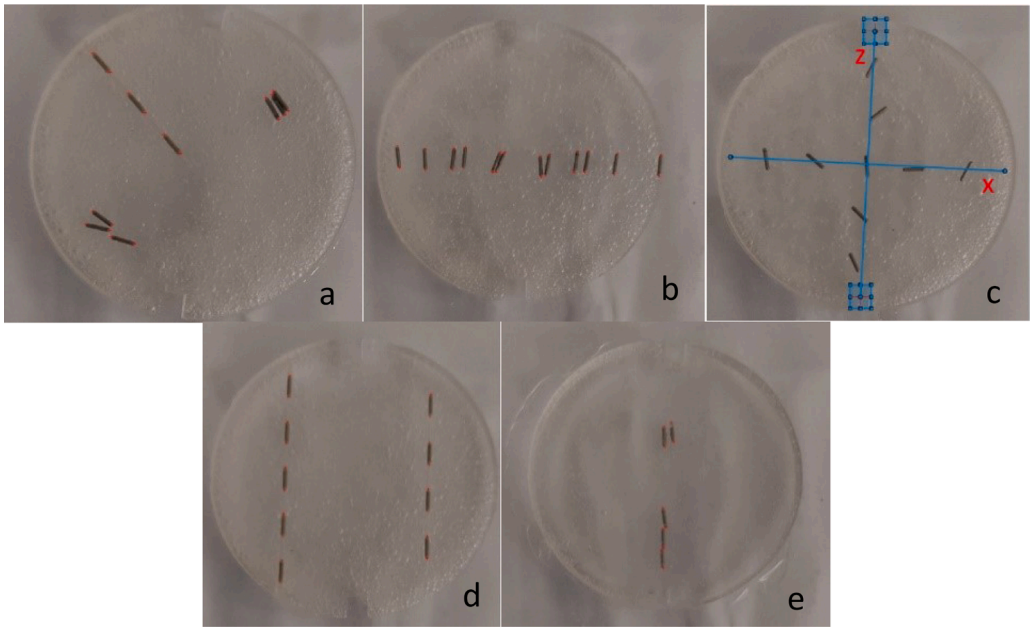


**Fig. 5.** Seed template arrangements to test clinical scenarios. (The notches for alignment are highlighted with a blue border in 'c' along with the local coordinate system). (a) Angled seeds (regularly spaced, clustered and touching), (b) Resolving seeds laterally, with different spacing and when placed at the periphery of the prostate, (c) Well-spaced angled seeds between 0° and 90°, (d) Regularly spaced seeds in a strand, (e) Seeds touching vertically in a row and horizontally.

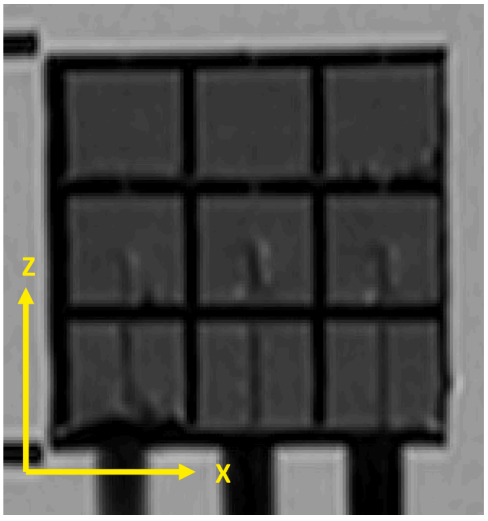


**Fig. 6.** Identifying geometrical position of needle tips relative to the edges of the grid.

The AAPM specifications for image guided robotized BT detail a spatial accuracy of 1 mm (SD 0.5 mm) for the placement of seeds in a phantom [3]. To achieve this, the spatial accuracy for needle tip identification should be $< 1$ mm. Our results show that is rarely achieved for the sequences evaluated in this study. This discrepancy is most pronounced for S2 (metal artefact correction). All sequences were acquired in the same scan session with no possibility of the needles shifting. Achieving a spatial accuracy of $< 1$ mm with the oblique needle at 45° to the Z-axis is also not achieved for all sequences. Theoretically better results are achievable by aligning the MR acquisition axis with the needle [18]. In practice this is likely to be time consuming if all needles are at different angles, which is particularly relevant for brachytherapy implants utilising a reduced number of entry points [19].

For future use of this phantom and analysis technique it would be advisable to use a jig to hold the camera at a fixed height and parallel to the gel discs, rather than doing this manually. This would reduce uncertainties from camera distortion. Furthermore, only a small selection of MR sequences were used in this study, and this is a known limitation. However, the work highlights the importance of sequence optimization for MR only prostate brachytherapy and has demonstrated some rules that could be utilized for MRI guided LDR prostate brachytherapy planning systems. The phantom described in this study could be used for future studies on different MRI scanners or to test new MRI protocols.

## 5. Conclusion

The phantom described in this paper has provided a method of verifying geometric seed and needle tip position in MRI, compared to their true position established a priori. Testing of clinically relevant arrangements for seed placement in T1 MRI sequences has shown that it is not always possible to identify the seeds within the desired accuracy suggested by the AAPM . The results have shown that using a metal artefact correction algorithm and a narrow slice width can help to improve the seed detection accuracy. However, for brachytherapy planning under MRI, it may be necessary to consider separate imaging sequences for needle tip detection and seed detection. Furthermore the results have demonstrated the need to avoid seeds in clusters and at the very edge of the prostate when planning using only MR imaging. For accurate seed detection it is essential to have a thorough understanding of the artefacts that may occur for the specific equipment being used. This work supports the need for continued developments in seed detection in MRI.

Eq. (2).

## Funding

This work has been co-funded by the European regional development Fund under EU Interreg 2 Seas, Grant 2S04-022.

## Ethical approval

Not required

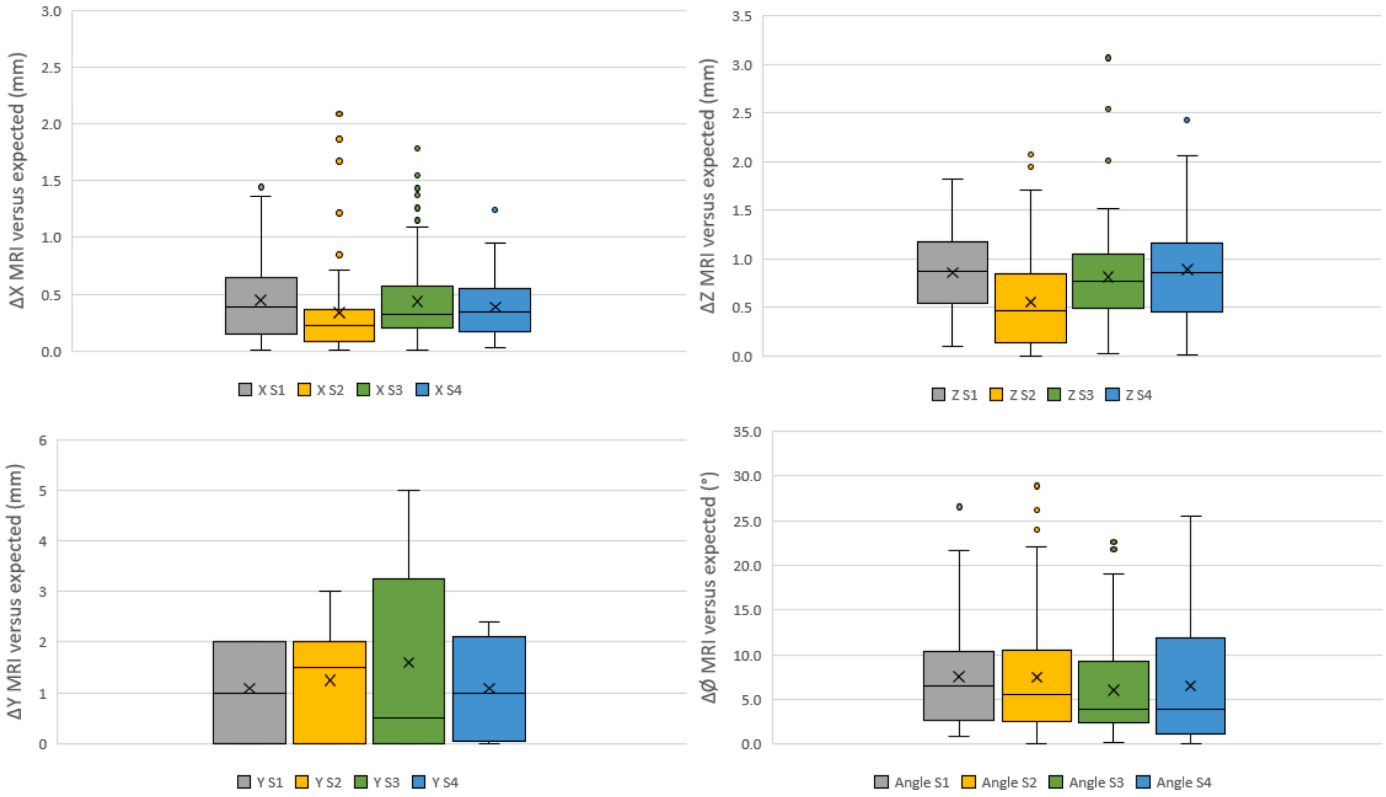


**Fig. 7.** Position and angle of all seeds in the four MRI sequences versus expected position from baseline photographs.

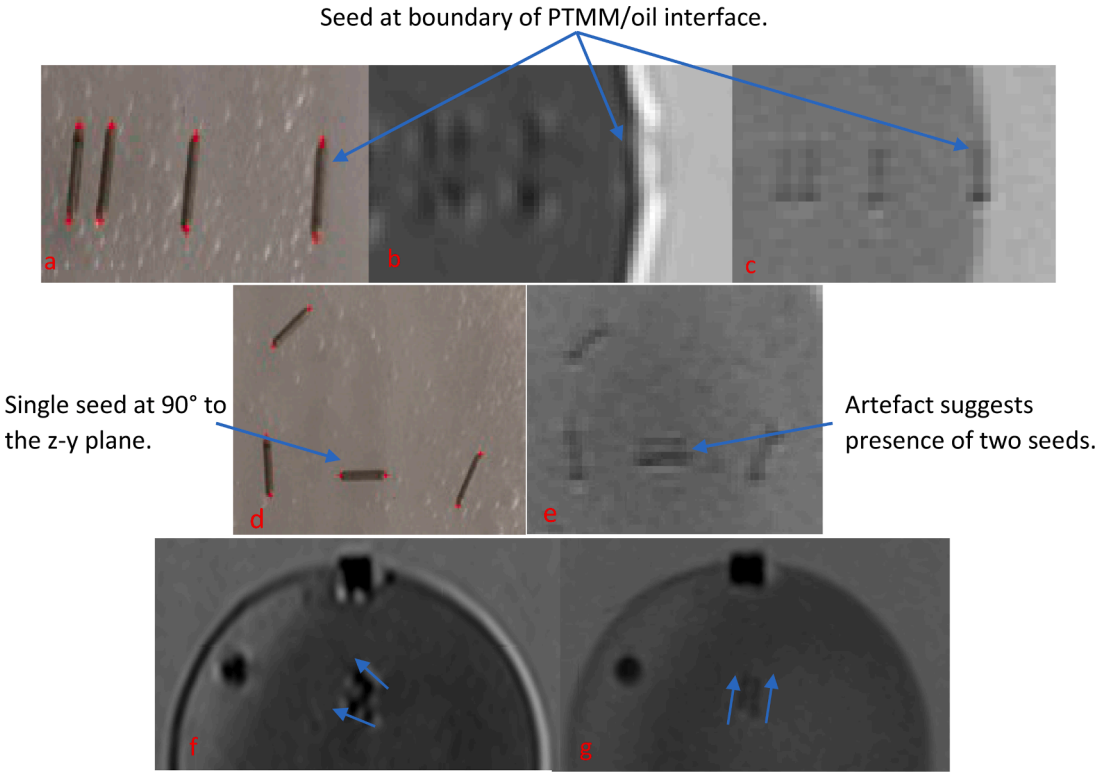


**Fig. 8.** A seed at the boundary of the PTMM/oil in the photo (a) very difficult to see in S4 (b) clearer in S2 (c). A seed at 90° could be mistaken in the MR images for two seeds, photo (d), S2 (e). Uncertainty in seed direction in (f) without metal artefact correction, compared to (g) with metal artefact correction.

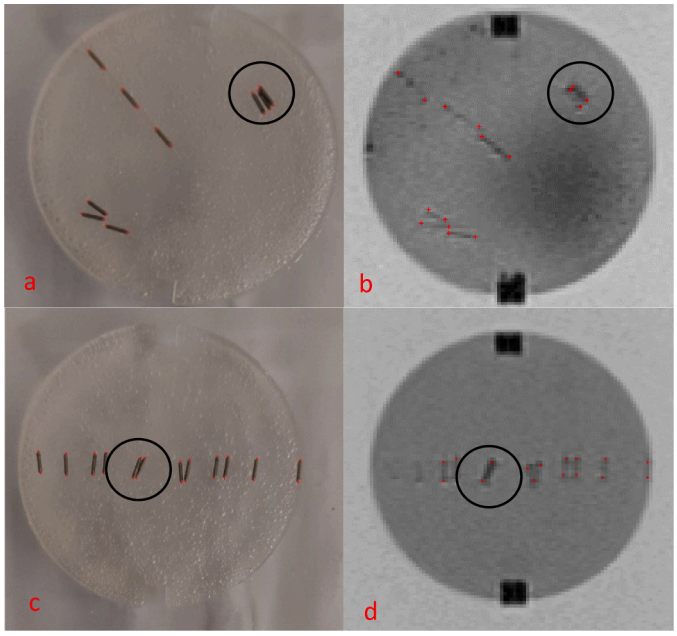


**Fig. 9.** Seed clusters with > 2 mm discrepancy in detected position in x or z illustrated on a photo (left) and S2 MRI (right).

## Conflicts of Interest

None

## Acknowledgments

With thanks to Mark Endaya, Colin Lupton and William Keeble at Portsmouth University for their contributions to manufacturing and 3D printing.

The authors are also grateful to the MRI radiographers at Portsmouth Hospital University Trust, for their time and expertise and to TUDelft for providing the Nitinol needles.

## References

[1] Prostate cancer diagnosis and management. National Institute for Health and Care Excellence. Prostate cancer: diagnosis and management - Clinical guideline [NG131]; doi: 10.1016/S0140-6736(96)07393-X.
[2] A. Polo, C. Salembier, J. Venselaar, et al., Review of intraoperative imaging and planning techniques in permanent seed prostate brachytherapy, Radiother. Oncol. (2010) 12–23.
[3] T.K. Podder, L. Beaulieu, B. Caldwell, et al., AAPM and GEC-ESTRO guidelines for image-guided robotic brachytherapy: report of task group 192, Med. Phys. 41 (2014) 101–501.
[4] K. Tanderup, A. Viswanathan, C. Kirisits, et al., MRI guided brachytherapy, Semin. Radiat. Oncol. 24 (2014) 181–191.
[5] S.S. Dhaliwal, T. Chettibi, S. Wilby, et al., Review of clinical and technological consideration for MRI-guided robotic prostate brachytherapy, IEEE Trans. Med. Robot. Bionics 3 (2021) 583–605, 1–1.
[6] H. Liu, A.J. Martin, C.L. Truwit, Interventional MRI at high-field (1.5 T): needle artifacts, J. Magn. Reson. Imaging 8 (1998) 214–219.
[7] R. Nosrati, A. Soliman, H. Safigholi, et al., MRI-based automated detection of implanted low dose rate (chytherapy seeds using quantitative susceptibility mapping (QSM) and unsupervised machine learning (ML), Radiother. Oncol. J. 129 (2018) 540–547.
[8] R. Nosrati, W.Y. Song, M. Wronski, et al., Feasibility of an MRI-only workflow for postimplant dosimetry of low-dose-rate prostate brachytherapy: transition from phantoms to patients, Brachytherapy 18 (2019) 863–874.
[9] K. Wachowicz, S.D. Thomas, B.G. Fallone, Characterization of the susceptibility artifact around a prostate brachytherapy seed in MRI, Med. Phys. 33 (2006) 4459–4467.
[10] S.D. Thomas, K. Wachowicz, B.G. Fallone, MRI of prostate brachytherapy seeds at high field: a study in phantom, Med. Phys. 36 (2009) 5228–5234.
[11] C.M.J. De Bazelaire, G.D. Duhamel, N.M. Rofsky, et al., MR imaging relaxation times of abdominal and pelvic tissues measured in vivo at 3.0 T: preliminary results, Radiology 230 (2004) 652–659.
[12] M. Stich, K. Schuller, A. Slawig, et al., Material Analysis for a New Kind of Hybrid Phantoms Utilized in Multimodal Imaging, Springer, Singapore, 2019, pp. 21–28.
[13] C. McGarry, L. Grattan, A. Ivory et al., Tissue mimicking materials for imaging and therapy phantoms: a review. Phys. Med. Biol. 65 (2020). doi: 10.1088/1361-6560/abbd17.
[14] J. Smith, C. Larson, Statistical approaches in surface finishing. Part 2. non-parametric methods for data analysis, Transactions of the IMF, 97 (2019) 1-10, 10.1080/00202967.2019.1555367.
[15] S.N. Bell Measurement Good Pactice Guide No. 11 (Issue 2). A Beginner's Guide to Uncertainty of Measurement.
[16] C.-.A.A. Collins Fekete, M. Plamondon, A.-.G.G. Martin, et al., Quantifying the effect of seed orientation in post-planning dosimetry of low-dose-rate prostate brachytherapy, Med. Phys. 41 (2014), 101704.
[17] D. Pfeiffer, S. Sutlief, W. Feng, et al., AAPM Task Group 128: quality assurance tests for prostate brachytherapy ultrasound systems, Med. Phys. 35 (2008) 5471–5489.
[18] C. Truwit, A.J. Martin, W.A. Hall, Clinical applications in various body regions, in: T Kahn, B Harald (Eds.), Interventional Magnetic Resonance Imaging, Springer, Berlin, 2012, pp. 97–111.
[19] S. Dhaliwal, S. Wilby, S. Firouzy, et al., CoBra robot for localized cancer treatment and diagnosis under real-time MRI, AUTOMED (2021). 10.1088/1361-6560/ab7633.